A Low-RCS, High-GBP Fabry–Perot Antenna With Embedded Chessboard Polarization Conversion Metasurface

ZHIMING LIU[1,2], **SHAOBIN LIU**[1], (Member, IEEE),
JENS BORNEMANN[2], (Life Fellow, IEEE),
XING ZHAO[1], **XIANGKUN KONG**[1], (Member, IEEE),
ZHENGYU HUANG[1], **BORUI BIAN**[1], **AND DONGDONG WANG**[3]

[1]College of Electronic and Information Engineering, Nanjing University of Aeronautics and Astronautics, Nanjing 210016, China
[2]Department of Electrical and Computer Engineering, University of Victoria, Victoria, BC V8W 2Y2, Canada
[3]China Ship Development and Design Center, Wuhan 430060, China

Corresponding author: Jens Bornemann (j.bornemann@ieee.org)

ABSTRACT A Fabry–Perot (FP) antenna with high gain-bandwidth product (GBP) and wideband radar cross section (RCS) reduction is proposed using an embedded chessboard polarization conversion metasurface (CPCM). A polarization conversion metasurface (PCM) unit and its mirror unit are etched on both sides of a dielectric substrate with chessboard arrangement to form a CPCM. The in-band and out-of-band low-RCS features of the FP antenna are realized by destructive interference, and the high GBP is attributed to the FP resonant cavity. Moreover, an additional small CPCM designed for another PCM unit is embedded into the original CPCM to construct an embedded CPCM, which helps to improve in-band RCS reduction and has a positive effect on gain enhancement and 10-dB impedance bandwidth. The measured results show that the FP antenna with embedded CPCM has a 10-dB return-loss bandwidth of 8.48-12.21 GHz (36.1%), a GBP of 1338, a 3-dB gain bandwidth of 8.9-11.5 GHz (25.5%) and a maximum realized gain of 17.2 dBi. Meanwhile, the measured RCS reduction band covers 8-26 GHz (105.9%) with a peak RCS reduction of 21.2 dB at 9.4 GHz.

INDEX TERMS Polarization conversion metasurface, Fabry–Perot antenna, high-gain, gain-bandwidth product, RCS reduction.

I. INTRODUCTION

Fabry–Perot antennas, also known as electromagnetic band gap (EBG) resonator antennas, Fabry–Perot resonator antennas, 2-D leaky-wave antennas, resonant cavity antennas and partially reflecting surface (PRS) antennas, have recently attracted considerable attention due to their highly directive radiation pattern and simple design [1]–[5]. The FP antenna was pioneered in the work of Von Trentini in 1956 [1]. Subsequently, a series of articles on FP antennas were published which contributed to the improvement of the FP antenna

The associate editor coordinating the review of this manuscript and approving it for publication was Santi C. Pavone.

performance in different aspects, including the optimization analysis [2]–[4], theoretical interpretation [5]–[8], and optimization design [9]–[12]. Many properties can be achieved with FP antennas, such as low profile [9], multi-band [10], circular polarization [11], RCS reduction [12], reconfigurable [13]–[15] and wideband [16] operation. With the rapid development in science and technology applications, wideband and RCS reduction properties of antennas play more important roles in many communications and sensor systems for some stealth platforms.

Nowadays, many achievements have been made in wideband FP antennas. The 10-dB return-loss bandwidth, gain enhancement, and gain-bandwidth product (GBP) of

FP antennas have been greatly improved. Frequency-selective surface (FSS)-based PRSs are usually employed to achieve wideband characteristics for FP antennas [15]–[24]. In [15]–[19], single-layer FSS-based PRSs are used to achieve relatively large GBPs for FP antennas. FP antennas with single-layer FSS-based PRSs have merits of simple assembly and low profile, but their GBPs (less than 672) should be further improved. In [20]–[24], multi-layer FSS-based PRSs are presented to improve the gain enhancement for FP antennas. Most of them obtain high gains, but the GBPs are not raised enough. Meanwhile, it is more difficult to extend the 10-dB return-loss bandwidth and 3-dB gain bandwidth of FP antennas by using multi-layer FSS-based PRSs due to increased design complexity.

All dielectric-based PRSs exhibit excellent capabilities in bandwidth expansion and wideband gain enhancement for FP antennas [25]–[40]. In [25]–[27], single-layer dielectric PRSs are employed to realize wide 3-dB gain bandwidths of FP antennas. Generally, single-layer dielectric PRS FP antennas achieve high GBPs by improving the radiation performance of the source antenna, which increases the design complexity of the source antenna. In [28]–[39], multi-layer dielectric PRSs are utilized to acquire high GBPs of FP antennas. Several types of multi-layer dielectric PRSs are adopted to ameliorate the radiation features of FP antennas, such as untruncated multi-layer dielectric PRSs [28], [29], truncated multi-layer dielectric PRSs [30]–[36], and transverse permittivity gradient (TPG) multi-layer dielectric PRSs [37]–[39]. Most of the multi-layer dielectric PRSs exhibit a strong capability in improving the GBP, but they may introduce higher longitudinal profiles compared with single-layer dielectric PRSs. Also, in [40], a near-field correcting structure (NFCS) all-dielectric PRS is used to optimize the wideband gain enhancement, which can locally modulate the phase of each correcting region of the antenna. Although the NFCS can effectively improve the GBP of the FP antenna, it also causes a large longitudinal profile.

Recently, metasurfaces have attracted tremendous attention in RCS reduction and bandwidth expansion for FP antennas due to their superior capability in electromagnetic wave modulation. In [12], [14], [41]–[44], low-RCS FP antennas are designed by constructing resistor-loaded absorbing surfaces (ASs) and PRSs. Although an FP antenna that is constructed by AS can obtain a wider RCS reduction band, its GBP is relatively low because some radiation energy of the antenna is absorbed by the AS. Chessboard arranged metasurfaces (CAMs) and polarization conversion metasurfaces (PCMs) are also exploited to reduce the RCS for FP antennas [45]–[48]. Both approaches depend on two FSS units with a reflection phase difference of $180° \pm 30°$ and etched on a single-layer dielectric substrate in a chessboard arrangement. From the mechanism of destructive interference, these methods have the potential to reduce the RCS over a wide band and improve gain enhancement. However, it can be observed in [45]–[48] that FP antennas designed with CAMs or PCMs fail to produce high GBPs. Therefore, it is

necessary to find a new approach to realize simultaneously wideband RCS reduction and high GBP for FP antennas.

In this paper, an embedded CPCM is proposed to achieve wideband low RCS and high GBP for an FP antenna. First, a CPCM is designed and investigated. The in-band and out-of-band low-RCS features of the FP antenna are determined by destructive interference, and the high GBP is attributed to the FP resonant cavity. Secondly, an additional small CPCM replaces the central tile of the CPCM to construct an embedded CPCM. The embedded CPCM can effectively improve in-band RCS reduction. Also, it has a positive effect on the gain enhancement and 10-dB return-loss bandwidth of the FP antenna. Measured results confirm the validity of the design which is presented in the following sections.

II. ANALYSIS OF POLARIZATION CONVERSION METASURFACE
A. DESIGN OF POLARIZATION CONVERSION METASURFACE

According to the theory of FP antennas, when the FP resonant condition (1) is satisfied, the cavity resonance between the CPCM and the ground of the source antenna can be excited, and the directivity of the FP antenna can be calculated by using (2) [1].

$$\varphi_{CPCM} = \frac{4\pi h_c}{c} f + 2N\pi - \varphi_{GND}, \quad N = 0, \pm 1, \pm 2 \ldots \quad (1)$$

$$D = D_p + 10 \log \left(\frac{1+R}{1-R} \right) \quad (2)$$

In (1) and (2), φ_{CPCM} and φ_{GND} represent the reflection phases of the CPCM and ground, respectively; h_c is the height of the cavity, and c is the speed of light. D and D_p denote the directivities of the FP antenna and source antenna, and R is the reflection amplitude of the CPCM. In order to design a high-gain FP antenna with a large 3-dB gain bandwidth, the reflection amplitude of the CPCM should be as large as possible, and a positive reflection phase gradient is required in the operating band [18].

A PCM unit and its mirror unit will be designed with chessboard layout to form the CPCM, which achieves both wideband FP resonance and RCS reduction for a wideband FP antenna. The positive reflection phase gradient band of the unit needs to match the operating band of the primary antenna in order to excite the FP resonance. The in-band RCS reduction of the FP antenna depends on the mutual cancellation of co-polarized reflected waves and co-polarized retransmitted waves of the PCM units, while the out-of-band RCS reduction is attributed to the polarization conversion characteristics of the PCM units. Also, the RCS reduction is related to the design of the CPCM. The number of CPCM tiles, the number of units that make up the tiles, and the arrangement method have an effect on the RCS reduction. Therefore, the design of the PCM unit structure is determined after considering various factors.
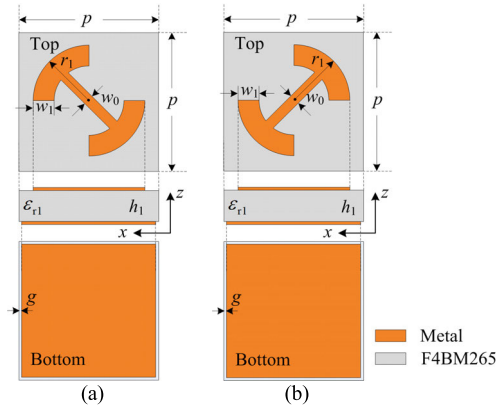
FIGURE 1. (a) PC$_{M1}$ unit, and (b) its mirror unit.

FIGURE 2. Schematic diagram of destructive interference.

FIGURE 3. Equivalent circuit of the PCM$_1$ (C_p = 0.15 pF, L_p = 0.00053 nH, L_v = 0.003 nH, C_v = 0.019 pF, C_m = 0.0015 pF, L_u = 2.16 nH, C_u = 0.039 pF, C_n = 0.0005 pF).

For this purpose, a PCM$_1$ unit and its mirror unit are designed. The PCM$_1$ unit is composed of a square metal patch and a dumbbell structure (Fig. 1). These units are etched on both sides of a F4BM265 (ε_{r1} = 2.65, tan δ = 0.0007) dielectric substrate. As the incident wave irradiates the PCM$_1$ along the +z direction, the square metal patch at the bottom of the PCM$_1$ exhibits the characteristic of a wide band positive reflection phase gradient, which improves the wideband gain enhancement for the antenna through the FP cavity resonance. As the incident wave irradiates the PCM$_1$ along the -z direction, the top structure can make the polarization conversion of the reflected wave in a wide band. The phase difference between the reflected waves of the PCM$_1$ unit and its mirror unit is 180°. The FP antenna to be designed uses destructive interference to achieve the wideband RCS reduction characteristic. As the phase difference between two waves traveling in the same direction is close to 180°±30°, destructive interference will occur [45]. Fig. 2 shows the operating mechanism of the destructive interference on the CPCM. After the PCM$_1$ and its mirror unit are arranged on a chessboard to form a CPCM, as the two incident waves irradiate the different units of the CPCM, the reflected waves will produce destructive interference because the phase difference of the two reflected waves is 180°; then the energy of the two reflected waves will be eliminated, thus achieving wideband RCS reduction for the FP antenna. All dimensions are optimized as follows: p = 4.8 mm, r_1 = 2.2 mm, w_0 = 0.5 mm, w_1 = 1.0 mm, g = 0.1 mm and h_1 = 3 mm.

The properties of the PCM$_1$ are analyzed by the equivalent circuit method (ECM) and CST simulations. Based on equivalent circuit theory, the PCM$_1$ exhibits dual diagonal symmetry that can be described by a four-port equivalent circuit [49]. The S-parameters are related to the four-port network; as a diagonal excitation is applied, the four-port network must be simplified to parallel admittances. When x or y polarized waves irradiate the PCM$_1$ along the -z direction, they will generate both field components of u and v incident polarizations. The equivalent circuit of the PCM$_1$ is depicted
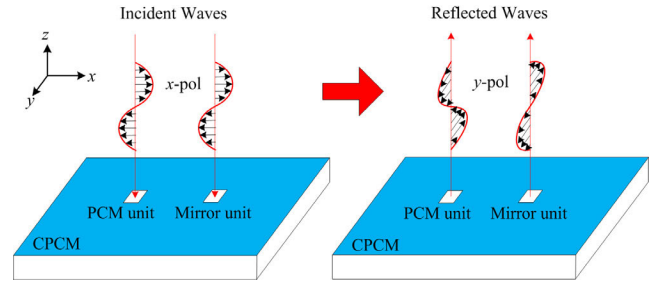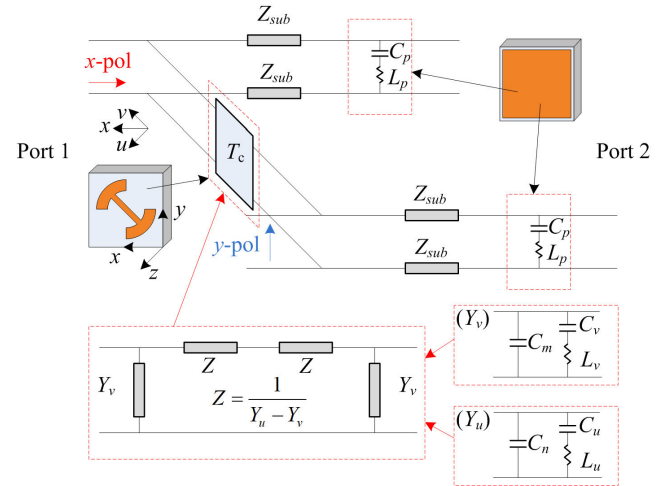
in Fig. 3. The bottom structure and dielectric of the PCM$_1$ are equivalent to an LC series circuit and a transmission line, respectively. The top structure is equivalent to connecting a quadripole matrix T_c, which transforms the polarization direction of the incident wave. The expression for T_c is

$$T_c = \begin{pmatrix} A & B \\ C & D \end{pmatrix} = \begin{pmatrix} \dfrac{Y_u + Y_v}{Y_u - Y_v} & \dfrac{2}{Y_u - Y_v} \\ \dfrac{2Y_uY_v}{Y_u - Y_v} & \dfrac{Y_u + Y_v}{Y_u - Y_v} \end{pmatrix} \quad (3)$$

where Y_u and Y_v are the parallel admittances in u and v directions.

$$Y_v = \frac{-2S_{11v}}{Z_{sub}S_{12v}}, \quad Y_u = \frac{-2S_{11u}}{Z_{sub}S_{12u}} \quad (4)$$

Fig. 4 shows the simulated configurations of the PCM$_1$ and its mirror unit. In the simulation process, the commercial software CST is used to analyze the properties of these unit cells. Two waveguide ports are set to solve for the reflection and transmission coefficients; Port 1 and Port 2 are positioned a distance of 15 mm away from the PCM$_1$. The magnetic and electric wall boundary conditions are enforced along the ±x- and ±y- directions, respectively. Fig. 5 presents the simulated and calculated results of the PCM$_1$. It can be observed that the simulated and calculated results coincide with each other.
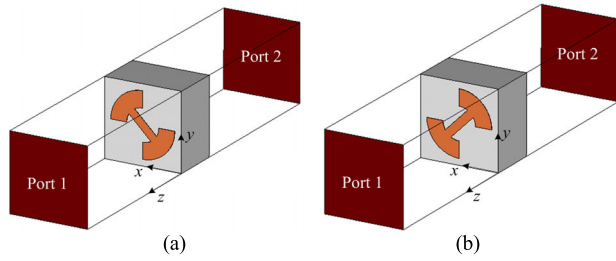
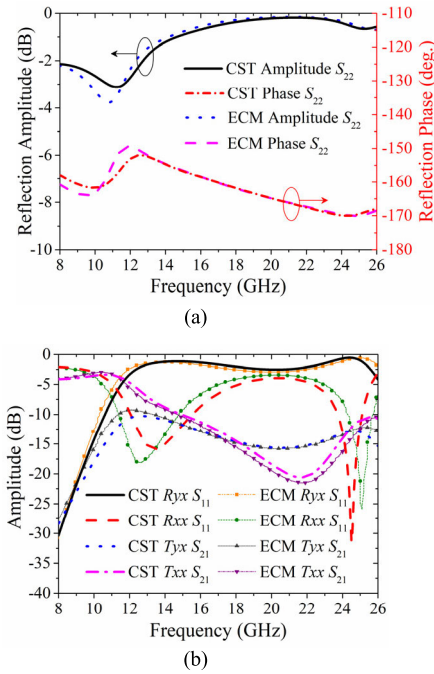**FIGURE 4.** Simulated configurations of (a) the PCM$_1$ unit and (b) its mirror unit.

FIGURE 6. Schematic diagram of low-RCS high-gain FP antenna.

FIGURE 5. Reflection and transmission coefficients of the PCM$_1$. (a) S_{22}, (b) S_{11}, S_{21}.

Fig. 5 (a) shows the reflection coefficient of the PCM$_1$ when the incident wave propagates along the $+z$ direction, with the simulated and calculated reflection amplitudes in black solid and blue dotted lines, the simulated and calculated reflection phases in red dash-dotted and magenta dashed lines. It shows that the PCM$_1$ has a positive reflection phase gradient band of 9.5-12.4 GHz, and the reflection amplitude is better than -3.7 dB in this band.

Fig. 5 (b) presents the reflection and transmission amplitudes of the co-polarized and cross-polarized waves when the x or y polarized wave irradiates the PCM$_1$ along the $-z$ direction. The simulated results of R_{yx}, R_{xx}, T_{yx}, and T_{xx} are in black solid, red dashed, blue dotted and magenta dash-dotted lines, while the calculated results of R_{yx}, R_{xx}, T_{yx}, and T_{xx} are in square orange dash-dotted, circle olive short dashed, up triangle dark gray short dotted, and down triangle purple short dash-dotted lines. It is illustrated that the reflection amplitude of the cross-polarized wave is better than -3.3 dB in the band of 12-26 GHz, thus the PCM$_1$ can achieve the
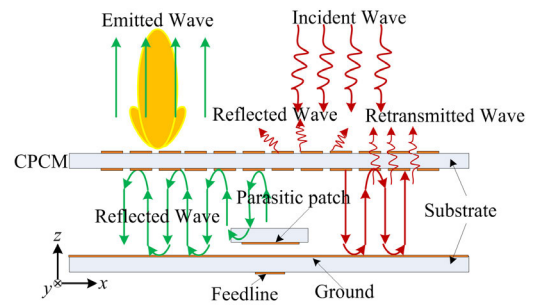
polarization conversion of the reflected wave in a wide band. Between 8 GHz and 11 GHz, the reflection amplitude of the co-polarized wave is greater than -7.11 dB. Also, it is shown that the transmission amplitude of the co-polarized wave is better than -3.42 dB over 8-11 GHz, and the transmission amplitude of the cross-polarized wave is below -9.27 dB in the entire frequency band. The simulated results of the mirror unit of the PCM$_1$ are the same as those of the PCM$_1$ unit. Therefore, when the incident waves irradiate the CPCM, which consists of the PCM$_1$ unit and its mirror unit, along the $-z$ direction, part of the waves will be reflected directly and the other parts transmitted into the cavity through the CPCM within the X-band. Concurrently, over 12-26 GHz, most of the incident waves will be reflected, and their polarization directions can be converted.

B. ANALYSIS OF LOW-RCS CHARACTERISTICS

Low-RCS antennas play an important role in defense applications. The RCS reduction mechanism of the FP antenna can be analyzed by ray theory, as shown in Fig. 6. In this design, the CPCM is used, and it is necessary to eliminate the co-polarized as well as the cross-polarized reflected waves of the CPCM. The co-polarized reflected wave can be consumed by the retransmitted wave which is formed by the incident wave transmitted into the FP cavity through the CPCM and retransmitted again after multiple reflections. The phase difference between the reflected waves and the retransmitted waves reflecting n times can be expressed as [45]

$$Dif_{\text{phase}} = (n+1)\varphi_{\text{t}} + (n-1)\varphi_{\text{r}} + 2nh_{\text{c}}k + n\varphi_{\text{GND}} \quad (5)$$

where φ_{t} and φ_{r} represent the transmission and reflection phase of the PCM, respectively; k is the wave vector in free space, and $\varphi_{\text{GND}} = \pi$ is the reflection phase of the metal ground of the source antenna. As the phase difference between the reflected wave and the retransmitted wave is close to $180°\pm30°$, destructive interference occurs between the retransmitted wave and the reflected wave.

Fig. 7 (a) shows the phase curves of the co-polarized reflected wave (S_{11}) and co-polarized transmitted wave (S_{21}) when the incident wave irradiates the PCM$_1$ along $-z$ direction. The phase difference between the reflected waves and the retransmitted waves can be calculated with (5) by means of the results obtained in Fig. 7 (b). It shows the
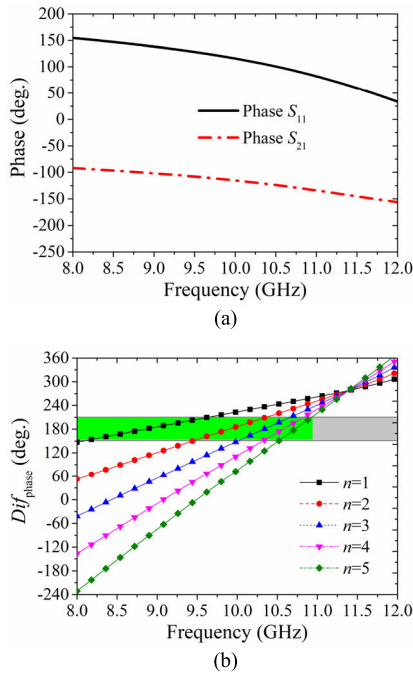
FIGURE 7. (a) Phases of the co-polarized reflected wave and the co-polarized transmitted wave. (b) Phase difference between the reflected waves and the first five retransmitted waves.

FIGURE 8. (a) Reflection phases and (b) phase difference between the reflection waves as the incident waves irradiate PCM_1 and its mirror along *-z* direction.

phase difference between reflected waves and the first five retransmitted waves. The green region indicates a phase difference of $180° \pm 30°$. The calculated results show that, over 8-10.9 GHz, the phase difference between the reflected waves and retransmitted waves is in the range of $180° \pm 30°$, thus destructive interference occurs between the retransmitted waves and the reflected waves to reduce the RCS of the FP antenna.

In addition, the PCM_1 and its mirror unit are etched on the dielectric substrate with chessboard arrangement to eliminate the reflected waves after the polarization direction of the reflected wave is converted. The reflection phases of the two units and the phase difference between the reflected waves, as the incident waves irradiate the PCM_1 and its mirror along the -z direction, are presented in Fig. 8. It shows that the PCM_1 and its mirror have perfect phase difference of $180°$ in a wide band. Therefore, over 12-26 GHz, the phase difference of reflected waves of two PCM units conforms to the principle of destructive interference so that the wideband RCS reduction of the FP antenna can be obtained due to the destructive interference of reflected waves.

The desired FP antenna operates in X-band. From the aforementioned analysis, the PCM_1 has high out-of-band polarization conversion efficiency. It can be found that the in-band RCS reduction is mainly attributed to the destructive interference between retransmitted and reflected waves, and the out-of-band RCS reduction is mainly determined by the polarization conversion properties of the PCM_1 and its mirror. Consequently, the CPCM, which consists of the PCM_1 unit and its mirror arranged in a chessboard, can reduce the in-band and out-of-band RCS over a wide band.
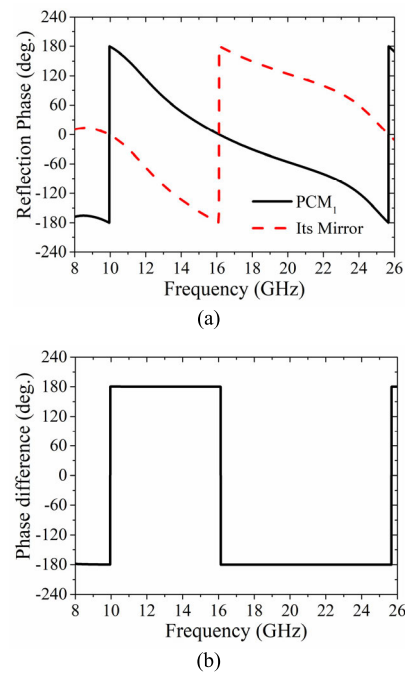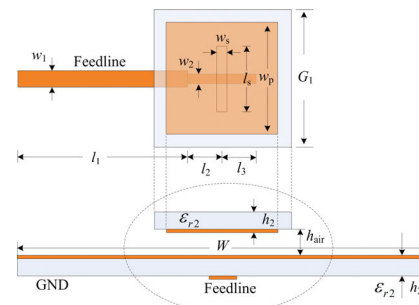

FIGURE 9. Slot-coupled patch antenna.

III. LOW–RCS FABRY–PEROT ANTENNA

A. PRIMARY ANTENNA

After the reflection and transmission coefficients of the CPCM are investigated, a slot-coupled patch antenna is designed as the source antenna (i.e., primary antenna) of the FP antenna, as shown in Fig. 9. The primary antenna is composed of a slot antenna and a parasitic patch. The metal ground and feedline of the slot antenna are etched on both sides of a F4BM220 ($\varepsilon_{r2} = 2.2$, $\tan \delta = 0.0007$) substrate with a thickness of $h_2 = 0.8$ mm. The length and width of the primary antenna are $W = 80$ mm. The parasitic patch is placed above the slot of the metal ground at the height of h_{air}. All structural parameters of the primary antenna are shown in Table 1. Fig. 10 shows the simulated results of the primary antenna which is seen to have a 10-dB impedance bandwidth of 8.99-11.55 GHz (24.9%), with a maximum realized gain of 9.14 dBi at 11.1 GHz. Its operating band
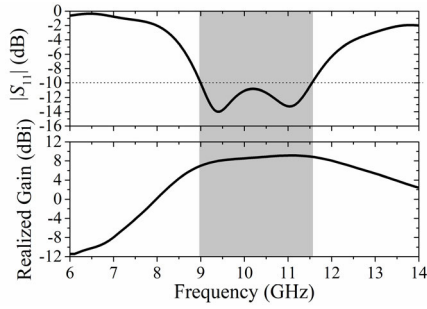
FIGURE 10. Simulated results of the primary antenna.

TABLE 1. Parameters of slot-coupled patch antenna.

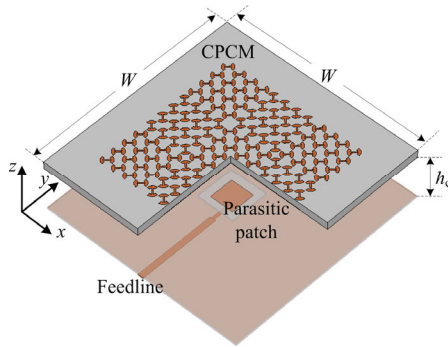| Parameters	h_2	h_{air}	l_1	l_2	l_3	l_s
Value (mm)	0.8	2.5	31.5	8.5	3	8.6
Parameters	G_1	w_p	w_d	w_{f1}	w_{f2}	w_s
Value (mm)	15	9.3	15	2.3	1.2	1

FIGURE 11. Fabry-Perot antenna with CPCM.

matches the positive reflection phase gradient band of the designed CPCM.

B. FABRY–PEROT ANTENNA WITH CPCM

The designed PCM_1 unit and its mirror are etched on the F4BM265 dielectric substrate ($\varepsilon_{r2} = 2.65$, $\tan\delta = 0.0007$) with a thickness of $h_1 = 3$ mm and a width of $W = 80$ mm in chessboard arrangement to form the CPCM. The CPCM is placed a distance h_c above the primary antenna, as shown in Fig. 11. The CPCM is composed of 3×3 tiles, and each tile consists of 4×4 PCM_1 units or its mirror units. The electromagnetic waves radiated by the primary antenna produce multiple reflections in the cavity and transmit through the CPCM along the $+z$ direction. When the height of the cavity and the reflection phase of the CPCM satisfy (1), the FP cavity resonance will be excited.

The cavity height has an important influence on the bandwidth and gain of the FP antenna. Fig. 12 and Table 2 show the simulated results of $|S_{11}|$ and the realized gain with different cavity heights. Table 2 shows that, as height h_c increases from 16.5 mm to 18.5 mm, the 10-dB return-loss bandwidth increases, and the corresponding 3-dB gain bandwidth
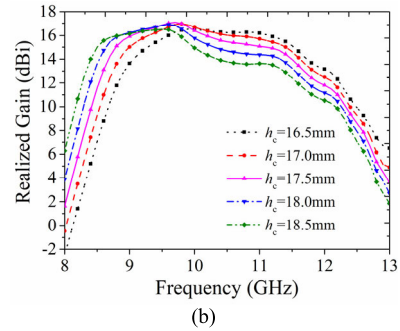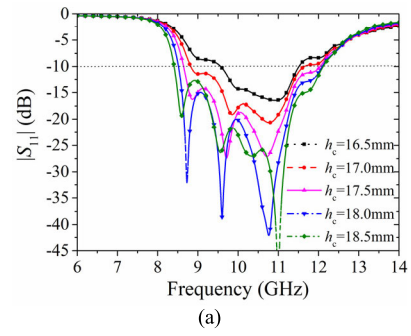

FIGURE 12. Simulated results of FP antenna loaded with the CPCM for different cavity heights. (a) $|S_{11}|$. (b) Realized gain.

TABLE 2. Comparison between Different cavity heights.

h_c (mm)	$|S_{11}|<$-10 dB	3-dB gain bandwidth	Maximum Gain (dBi)	GBP
16.5	9.57-11.51GHz (18.1%)	8.99-11.85GHz (27.4%)	16.53 (9.9 GHz)	1232
17.0	8.83-11.65GHz (27.5%)	8.84-11.63GHz (27.3%)	16.96 (9.8 GHz)	1356
17.5	8.65-12.05GHz (32.9%)	8.68-11.48GHz (27.8%)	17.09 (9.7 GHz)	1422
18.0	8.52-12.09GHz (34.6%)	8.53-11.34GHz (28.3%)	16.90 (9.6 GHz)	1386
18.5	8.41-12.11GHz (36.1%)	8.37-11.19GHz (28.8%)	16.52 (9.5 GHz)	1292

expands, while the maximum gain and GBP are increased first and then decreased. After comprehensive consideration, $h_c = 17.5$ mm is selected. In this case, the FP antenna has a 10-dB return-loss bandwidth of 8.65-12.05 GHz (32.9%), a peak directivity of 17.28 dBi at 9.7 GHz, and a GBP of 1422.

From the above analysis, the 10-dB return-loss bandwidth of the antenna expands from 24.9% to 32.9%, and the maximum realized gain increases from 9.14 dBi (11.1 GHz) to 17.09 dBi (9.7 GHz). The bandwidth expansion of the antenna is attributed to the introduction of two additional resonance peaks after the CPCM loading. Meanwhile, the gain enhancement can be explained by (2). For example, at 9.7 GHz, the directivity of the primary antenna is $D_p = 8.75$ dBi, the reflection amplitude of the PCM1 is $R = 0.74$, so the directivity of the FP antenna can be calculated
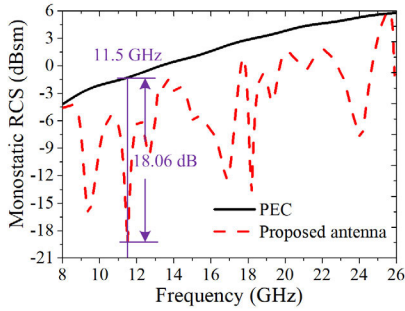
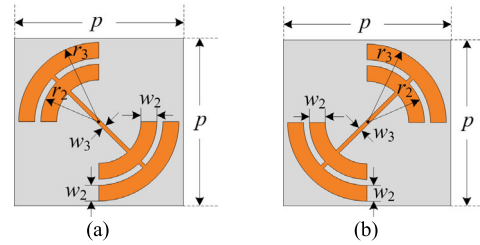FIGURE 13. Monostatic RCS of FP antenna with CPCM.

FIGURE 14. (a) The PCM$_2$ unit, and (b) its mirror unit.

FIGURE 15. Schematic diagram of embedded CPCM.

FIGURE 16. Reflection and transmission coefficients of PCM$_2$. (a) S_{22}, (b) S_{11}, S_{21}.

as D = 17.05 dBi which agrees well with the simulated directivity. In addition, as shown in Fig. 13, the FP antenna has a wideband RCS reduction property over 8-26 GHz, and a peak RCS reduction of 18.06 dB at 11.5 GHz.

C. FABRY–PEROT ANTENNA WITH EMBEDDED CPCM

The X-band was widely used in stealth radars, such as airborne radar [50], [51], shipborne radar [52], [53], and air defense radar [54]. Its relative short wavelength enables higher resolution imaging for target identification and discrimination [55], [56]. For better stealth, improving the in-band RCS reduction of the designed FP antenna is an important issue. From Section II, the in-band RCS reduction is mainly caused by the destructive interference between the retransmitted and reflected waves. As shown in Fig. 5, in the 8-12 GHz range, the co-polarized reflection amplitude of PCM$_1$ towards lower frequencies is larger than that of the co-polarized transmission, while the co-polarized reflection amplitude towards higher frequencies is smaller than that of the co-polarized transmission. In order to improve the in-band RCS reduction of the FP antenna, it is necessary to improve the in-band energy balance of the co-polarized reflected and co-polarized transmitted waves of the CPCM. For this purpose, the PCM$_2$ unit and the embedded CPCM are designed, as presented in Fig. 14 and Fig. 15. Due to the consideration of reducing the effect of the small CPCM on the FP antenna performance, a small CPCM replaces the central tile of the original CPCM to form the embedded CPCM. The small CPCM is composed of 2×2 small tiles, and each small tile consists of 2×2 PCM$_2$ units or its mirror units. The optimized parameters of the PCM$_2$ unit are as follows: p = 4.8 mm, r_2 = 1.6 mm, r_3 = 2.3 mm, w_2 = 0.6 mm, w_3 = 0.1 mm.

Fig. 16 shows the simulated results of the reflection and transmission coefficients of the PCM$_2$. Fig. 16 (a) presents the reflection coefficient when incident waves propagate along the $+z$ direction, with the reflection amplitude in black solid line and reflection phase in red dash-dotted line. It shows that the PCM$_2$ has a positive reflection phase gradient characteristic in the band of 8.4-9.4 GHz, and the reflection amplitude is greater than -8.97 dB. Compared with the PCM$_1$, the positive reflection phase gradient band of the
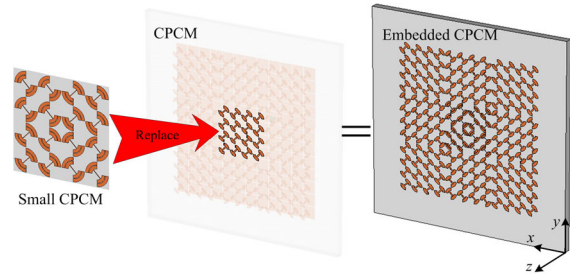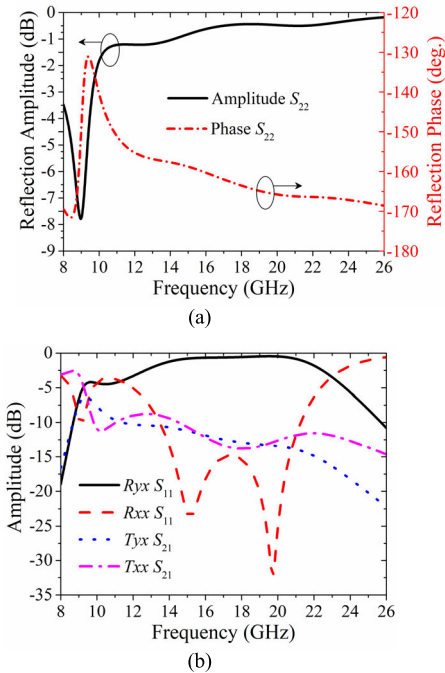
PCM$_2$ moves towards the low-frequency direction, and the reflection amplitude decreases in the low-frequency band. Obviously, around 10 GHz, the reflection amplitude of the embedded CPCM is larger than that of the CPCM, which contributes to improving the gain enhancement. Fig. 16 (b) shows the reflection and transmission amplitudes of the co-polarized and cross-polarized wave when the linearly polarized wave irradiates the PCM$_2$ along the -z direction, R_{yx} in black solid, R_{xx} in the red dashed, T_{yx} in blue dotted and T_{xx} in magenta dash-dotted lines. It can be seen that the reflection

FIGURE 17. Monostatic RCS of the FP antenna with embedded CPCM.

FIGURE 18. Comparison of simulated results. (a) $|S_{11}|$, (b) realized gain.

FIGURE 19. Measurement scenario of the prototype.

FIGURE 20. Measured results of the improved FP antenna. (a) $|S_{11}|$, (b) realized gain.
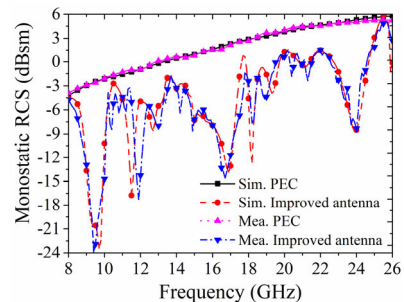
FIGURE 21. Measured monostatic RCS of the improved FP antenna.
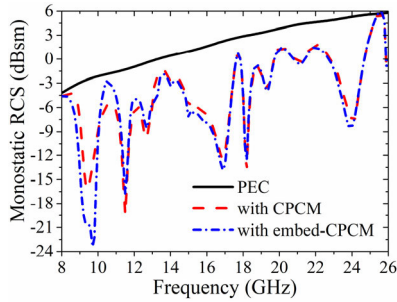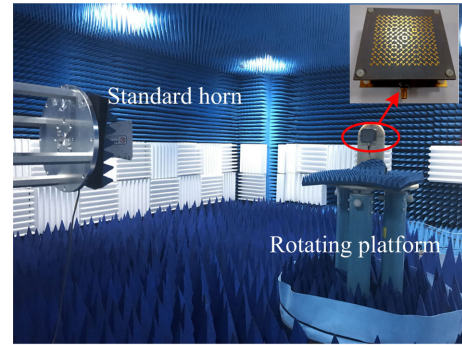
amplitude of the cross-polarized with reflected wave of the PCM$_2$ is better than -3.33 dB in the band of 12-22.93 GHz. In the 8-12 GHz range, the co-polarized reflection amplitude of the PCM$_2$ towards lower frequencies is smaller than that of the co-polarized transmission, while the co-polarized reflection amplitude towards higher frequencies is larger than that of the co-polarized transmission. After embedding the small CPCM into the CPCM, the energy of co-polarized reflection and co-polarized transmission of the embedded CPCM are more balanced, so that the retransmitted waves and reflected waves cancel each other more thoroughly.

The performance of the FP antenna with the embedded CPCM is investigated. Fig. 17 shows the monostatic RCS of the improved FP antenna. It can be seen that the RCS reduction of the improved FP antenna has been significantly improved in the band of 8.0-10.1 GHz; the maximum RCS reduction is 21.06 dB at 9.7 GHz, while the RCS reduction of the antenna decreases in the band of 10.1-11.1 GHz. This is essentially due to the increase of the transmission

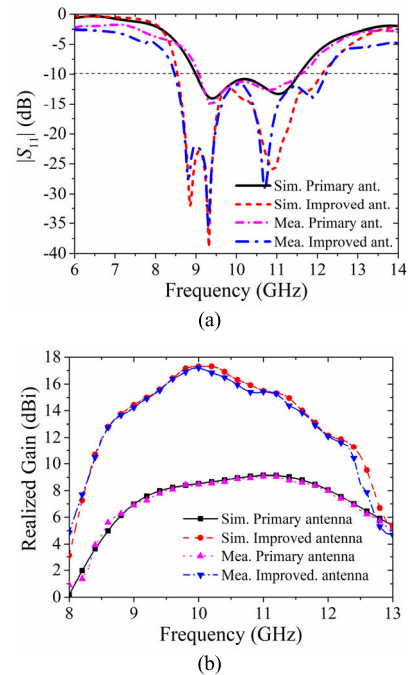amplitude of the co-polarized wave around 9 GHz and the decrease of the transmission amplitude around 10.5 GHz when the incident waves irradiate the embedded CPCM along the *-z* direction. Also, the simulated RCS result shows that the

TABLE 3. Comparison between the designed antenna and existing works.

Ref.	Structure of PRS	10-dB impedance bandwidth (GHz)	3-dB gain bandwidth (GHz)	Maximum Realized Gain (dBi)	RCS reduction band (GHz)	GBP	Area (λ_0^2)
[6]	Thin metallic FSS layer	-	5%	16.3	-	213	12×12
[8]	One-layer PRS	About 17.3%	27.4%	13.6	-	628	3.2×3.2
[27]	One-layer PRS + AS	Average 4%	Average 6%	13.6	8-14 (54.5%)	137	~2.94×~2.94
[28]	One-layer PRS + AS	11.2-12 (6.9%)	11.2-11.62 (3.7%)	13.2	6-14 (80%)	77.3	2.32×2.32
[30]	Two-layer PRS + AS	6.02-6.63 (10.2%)	About 9.5%	14.4	8-18 (76.9%)	262	2.47×2.47
[32]	One-layer PRS + AS	7.25-8.1 (11.1%)	About 7.9%	12.3	5-13 (88.9%)	134	2.56×2.56
[33]	One-layer CAM	9.42-11.35 (18.6%)	16.58%	About 11.8	8-18 (76.9%)	251	2.20×2.20
[34]	One-layer CAM	9.08-9.86 (8.4%)	14.3%	13.2	8-14 (54.5%)	299	2.83×2.83
[35]	One-layer PCM	8.25-9.5 (14.1%)	About 11.1%	11.2	6-14 (80%)	146	2.20×2.20
[36]	One-layer PCM	9.2-10.1 (8.8%)	About 12.4%	About 12	9-20 (75.9%)	197	1.25×1.25
This work	One-layer Embedded CPCM	8.48-12.21 (36.1%)	8.9-11.5 (25.5%)	17.2	8-26 (105.9%)	1338	2.76×2.76

Note: GBP=BW×$10^{G/10}$, where BW denotes the 3-dB gain bandwidth, G denotes the maximum realized gain. λ_0 denotes the wavelength at the center frequency of the effective bandwidth in free space.
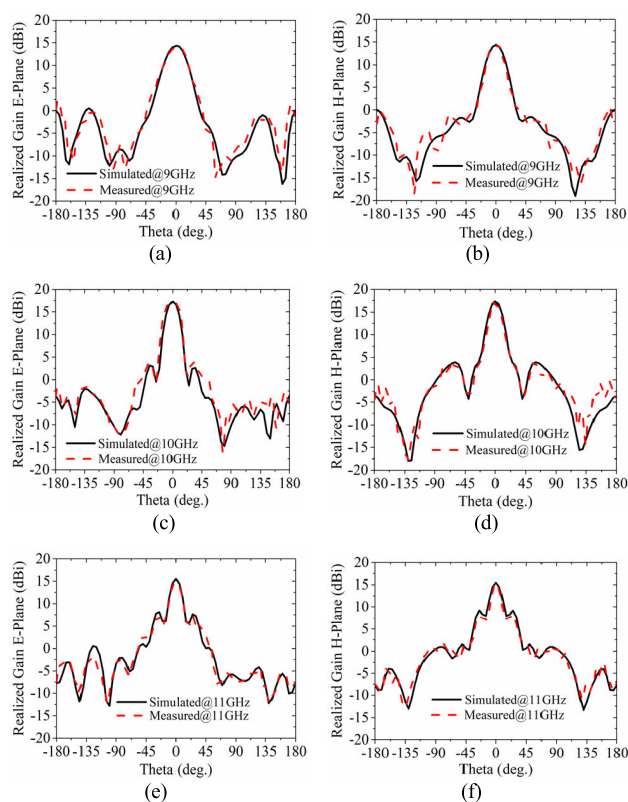

FIGURE 22. Measured radiation patterns of the improved FP antenna. (a) E-plane and (b) H-plane at 9 GHz, (c) E-plane and (d) H-plane at 10 GHz, (e) E-plane and (f) H-plane at 11 GHz.

1362. Compared with the primary FP antenna, the improved FP antenna has a wider 10-dB return-loss bandwidth and a larger maximum realized gain, but the 3-dB gain bandwidth decreases, so the GBP decreases. The 10-dB return-loss bandwidth expansion of the improved FP antenna is mainly due to the higher Q value that can be obtained by the centrally embedded small CPCM. The narrower 3-dB gain bandwidth of the improved FP antenna is caused by the fact that the gain becomes lower in the low-frequency band and higher in the high-frequency band. This is principally due to the centrally embedded small CPCM which improves the transmission amplitude of the CPCM in the low-frequency operating band and enhances the reflection amplitude of the CPCM in the high-frequency operating band. Moreover, the reflection amplitude of the embedded CPCM is larger than that of the original CPCM around 10 GHz, which makes the embedded CPCM contribute more to gain improvement.

IV. EXPERIMENTAL RESULTS

The FP antenna with embedded CPCM has been fabricated and measured. The prototype consists of a slot-coupled patch antenna and a substrate etched with the embedded CPCM. The slot-coupled patch antenna is etched on an F4BM220 substrate with thickness of 0.8 mm, and the embedded CPCM is etched on an F4BM265 dielectric substrate with thickness of 3 mm, length and width of $W = 80$ mm. The overall size of the fabricated antenna is 80 mm × 80 mm × 21.3 mm. All measurements were performed in a microwave anechoic chamber as shown in Fig. 19.

Fig. 20 shows the measured results of $|S_{11}|$ and realized gain for the improved FP antenna. The improved FP antenna has a measured 10-dB impedance bandwidth of 8.48-12.21 GHz (36.1%), a measured 3-dB gain bandwidth of 8.9-11.5 GHz (25.5%) and a measured maximum realized gain of 17.2 dBi at 10.0 GHz. These values agree very well with simulations. The measured monostatic RCS of the improved FP antenna is shown in Fig. 21. It shows that

impact of the embedded CPCM on the out-of-band RCS can be neglected.

The simulated results of $|S_{11}|$ and the realized gain of the improved FP antenna are displayed in Fig. 18 where Fig. 18 (a) and Fig. 18 (b) show that the improved FP antenna has a 10-dB return-loss bandwidth of 8.55-12.11 GHz (34.5%), a 3-dB gain bandwidth of 8.95-11.54 GHz (25.3%), a maximum realized gain of 17.31 dBi at 10.2 GHz and a GBP of

the FP antenna with embedded CPCM has an RCS reduction band of 8-26 GHz and a peak RCS reduction value of 21.2 dB at 9.4 GHz.

The simulated and measured radiation patterns at 9 GHz, 10 GHz and 11 GHz are depicted in Fig. 22. These patterns show that the improved FP antenna has good radiation directivity. Also, the half-power beam widths (HPBWs) of the FP antenna in the E-plane and H-plane at 10.0 GHz are 21.5° and 21.7°, respectively. The measurements confirm the correctness of this design. Table 3 exhibits the performances comparison between the proposed antenna and related reports. It illustrates that the FP antenna with embedded CPCM has excellent performance, including a wider 10-dB return-loss bandwidth, a larger gain enhancement, a wider RCS reduction band and a higher GBP.

V. CONCLUSION

A high gain-bandwidth product Fabry–Perot antenna with wideband RCS reduction property is proposed using the embedded CPCM. An FP antenna with CPCM is designed and investigated. The mechanisms of the in-band and out-of-band RCS reductions are analyzed. They reveal that the in-band RCS reduction of the FP antenna is mainly attributed to the destructive interference between retransmitted waves and reflected waves, and the out-of-band RCS reduction is mainly determined by the polarization conversion characteristics of the CPCM. The high GBP depends on the FP resonant cavity. Moreover, an additional small CPCM replaces the central tile of the original CPCM to form the embedded CPCM. The embedded CPCM improves the in-band RCS reduction for the FP antenna. Also, it has a positive effect on gain enhancement and 10-dB impedance bandwidth expansion. Experiments show that the FP antenna with the embedded CPCM has a relative 10-dB return-loss bandwidth of 36.1%, a GBP of 1338, a 3-dB gain bandwidth of 25.5%, and a maximum gain of 17.2 dBi at 10 GHz. Meanwhile, the measured RCS reduction band of the proposed FP antenna covers 8-26 GHz (105.9%), with a peak RCS reduction of 21.2 dB at 9.4 GHz.

REFERENCES

[1] G. V. Trentini, "Partially reflecting sheet arrays," *IRE Trans. Antennas Propag.*, vol. 4, no. 4, pp. 666–671, Oct. 1956.

[2] A. P. Feresidis and J. C. Vardaxoglou, "High gain planar antenna using optimised partially reflective surfaces," *IEE Proc. Microw., Antennas Propag.*, vol. 148, no. 6, pp. 345–350, Dec. 2001.

[3] G. Lovat, P. Burghignoli, and D. R. Jackson, "Fundamental properties and optimization of broadside radiation from uniform leaky-wave antennas," *IEEE Trans. Antennas Propag.*, vol. 54, no. 5, pp. 1442–1452, May 2006.

[4] D. R. Jackson, P. Burghignoli, G. Lovat, F. Capolino, J. Chen, D. R. Wilton, and A. A. Oliner, "The fundamental physics of directive beaming at microwave and optical frequencies and the role of leaky waves," *Proc. IEEE*, vol. 99, no. 10, pp. 1780–1805, Oct. 2011.

[5] D. R. Jackson and A. A. Oliner, "A leaky-wave analysis of the high-gain printed antenna configuration," *IEEE Trans. Antennas Propag.*, vol. 36, no. 7, pp. 905–910, Jul. 1988.

[6] A. T. Almutawa, A. Hosseini, D. R. Jackson, and F. Capolino, "Leaky-wave analysis of wideband planar Fabry–Pérot cavity antennas formed by a thick PRS," *IEEE Trans. Antennas Propag.*, vol. 67, no. 8, pp. 5163–5175, Aug. 2019.

[7] T. Zhao, D. R. Jackson, J. T. Williams, and A. A. Oliner, "General formulas for 2-D leaky-wave antennas," *IEEE Trans. Antennas Propag.*, vol. 53, no. 11, pp. 3525–3533, Nov. 2005.

[8] A. Hosseini, F. De Flaviis, and F. Capolino, "Design formulas for planar Fabry–Pérot cavity antennas formed by thick partially reflective surfaces," *IEEE Trans. Antennas Propag.*, vol. 64, no. 12, pp. 5487–5491, Dec. 2016.

[9] Y. Sun, Z. N. Chen, Y. Zhang, H. Chen, and T. S. P. See, "Subwavelength substrate-integrated Fabry–Pérot cavity antennas using artificial magnetic conductor," *IEEE Trans. Antennas Propag.*, vol. 60, no. 1, pp. 30–35, Jan. 2012.

[10] B. A. Zeb, Y. Ge, K. P. Esselle, Z. Sun, and M. E. Tobar, "A simple dual-band electromagnetic band gap resonator antenna based on inverted reflection phase gradient," *IEEE Trans. Antennas Propag.*, vol. 60, no. 10, pp. 4522–4529, Oct. 2012.

[11] F. Qin, S. Gao, G. Wei, Q. Luo, C. Mao, C. Gu, J. Xu, and J. Li, "Wideband circularly polarized Fabry–Pérot antenna [Antenna applications Corner]," *IEEE Antennas Propag. Mag.*, vol. 57, no. 5, pp. 127–135, Oct. 2015.

[12] H. Jiang, Z. Xue, W. Li, W. Ren, and M. Cao, "Low-RCS high-gain partially reflecting surface antenna with metamaterial ground plane," *IEEE Trans. Antennas Propag.*, vol. 64, no. 9, pp. 4127–4132, Sep. 2016.

[13] R. Guzmán-Quirós, A. R. Weily, J. L. Gómez-Tornero, and Y. J. Guo, "A Fabry–Pérot antenna with two-dimensional electronic beam scanning," *IEEE Trans. Antennas Propag.*, vol. 64, no. 4, pp. 1536–1541, Apr. 2016.

[14] C. Huang, W. Pan, X. Ma, and X. Luo, "A frequency reconfigurable directive antenna with wideband low-RCS property," *IEEE Trans. Antennas Propag.*, vol. 64, no. 3, pp. 1173–1178, Mar. 2016.

[15] R. Lian, Z. Tang, and Y. Yin, "Design of a broadband polarization-reconfigurable Fabry–Pérot resonator antenna," *IEEE Antennas Wireless Propag. Lett.*, vol. 17, no. 1, pp. 122–125, Jan. 2018.

[16] N. Wang, Q. Liu, C. Wu, L. Talbi, Q. Zeng, and J. Xu, "Wideband Fabry–Pérot resonator antenna with two complementary FSS layers," *IEEE Trans. Antennas Propag.*, vol. 62, no. 5, pp. 2463–2471, May 2014.

[17] Z. G. Liu, Z. X. Cao, and L. N. Wu, "Compact low-profile circularly polarized Fabry–Pérot resonator antenna fed by linearly polarized microstrip patch," *IEEE Antennas Wireless Propag. Lett.*, vol. 15, pp. 524–527, Jul. 2016.

[18] Y. Ge, K. P. Esselle, and T. S. Bird, "The use of simple thin partially reflective surfaces with positive reflection phase gradients to design wideband, low-profile EBG resonator antennas," *IEEE Trans. Antennas Propag.*, vol. 60, no. 2, pp. 743–750, Feb. 2012.

[19] W. Cao, X. Lv, Q. Wang, Y. Zhao, and X. Yang, "Wideband circularly polarized Fabry–Pérot resonator antenna in ku-band," *IEEE Antennas Wireless Propag. Lett.*, vol. 18, no. 4, pp. 586–590, Apr. 2019.

[20] C. Mateo-Segura, A. P. Feresidis, and G. Goussetis, "Bandwidth enhancement of 2-D leaky-wave antennas with double-layer periodic surfaces," *IEEE Trans. Antennas Propag.*, vol. 62, no. 2, pp. 586–593, Feb. 2014.

[21] P.-Y. Qin, L.-Y. Ji, S.-L. Chen, and Y. J. Guo, "Dual-polarized wideband Fabry–Pérot antenna with quad-layer partially reflective surface," *IEEE Antennas Wireless Propag. Lett.*, vol. 17, no. 4, pp. 551–554, Apr. 2018.

[22] M. L. Abdelghani, H. Attia, and T. A. Denidni, "Dual- and wideband Fabry–Pérot resonator antenna for WLAN applications," *IEEE Antennas Wireless Propag. Lett.*, vol. 16, pp. 473–476, Jun. 2017.

[23] K. Konstantinidis, A. P. Feresidis, and P. S. Hall, "Broadband sub-wavelength profile high-gain antennas based on multi-layer metasurfaces," *IEEE Trans. Antennas Propag.*, vol. 63, no. 1, pp. 423–427, Jan. 2015.

[24] K. Konstantinidis, A. P. Feresidis, and P. S. Hall, "Multilayer partially reflective surfaces for broadband Fabry–Pérot cavity antennas," *IEEE Trans. Antennas Propag.*, vol. 62, no. 7, pp. 3474–3481, Jul. 2014.

[25] F. Wu and K. M. Luk, "Wideband high-gain open resonator antenna using a spherically modified, second-order cavity," *IEEE Trans. Antennas Propag.*, vol. 65, no. 4, pp. 2112–2116, Apr. 2017.

[26] L.-Y. Ji, P.-Y. Qin, and Y. J. Guo, "Wideband Fabry–Pérot cavity antenna with a shaped ground plane," *IEEE Access*, vol. 6, pp. 2291–2297, 2018.

[27] H. H. Tran and I. Park, "Compact wideband circularly polarised resonant cavity antenna using a single dielectric superstrate," *IET Microw., Antennas Propag.*, vol. 10, no. 7, pp. 729–736, May 2016.

[28] N. Wang, J. Li, G. Wei, L. Talbi, Q. Zeng, and J. Xu, "Wideband Fabry–Pérot resonator antenna with two layers of dielectric superstrates," *IEEE Antennas Wireless Propag. Lett.*, vol. 14, pp. 229–232, 2015.

[29] N. Wang, L. Talbi, Q. Zeng, and J. Xu, "Wideband Fabry–Pérot resonator antenna with electrically thin dielectric superstrates," *IEEE Access*, vol. 6, pp. 14966–14973, 2018.

[30] B. A. Zeb, R. M. Hashmi, and K. P. Esselle, "Wideband gain enhancement of slot antenna using one unprinted dielectric superstrate," *Electron. Lett.*, vol. 51, no. 15, pp. 1146–1148, Jul. 2015.

[31] R. M. Hashmi and K. P. Esselle, "A wideband EBG resonator antenna with an extremely small footprint area," *Microw. Opt. Technol. Lett.*, vol. 57, no. 7, pp. 1531–1535, Jul. 2015.

[32] R. M. Hashmi, B. A. Zeb, and K. P. Esselle, "Wideband high-gain EBG resonator antennas with small footprints and all-dielectric superstructures," *IEEE Trans. Antennas Propag.*, vol. 62, no. 6, pp. 2970–2977, Jun. 2014.

[33] A. Lalbakhsh, M. U. Afzal, K. P. Esselle, S. L. Smith, and B. A. Zeb, "Single-dielectric wideband partially reflecting surface with variable reflection components for realization of a compact high-gain resonant cavity antenna," *IEEE Trans. Antennas Propag.*, vol. 67, no. 3, pp. 1916–1921, Mar. 2019.

[34] R. M. Hashmi and K. P. Esselle, "Enhancing the performance of EBG resonator antennas by individually truncating the superstructure layers," *IET Microw., Antennas Propag.*, vol. 10, no. 10, pp. 1048–1055, Jul. 2016.

[35] N. Nguyen-Trong, H. H. Tran, T. K. Nguyen, and A. M. Abbosh, "A compact wideband circular polarized Fabry–Pérot antenna using resonance structure of thin dielectric slabs," *IEEE Access*, vol. 6, pp. 56333–56339, 2018.

[36] N. Nguyen-Trong, H. H. Tran, T. K. Nguyen, and A. M. Abbosh, "Wideband Fabry–Pérot antennas employing multilayer of closely spaced thin dielectric slabs," *IEEE Antennas Wireless Propag. Lett.*, vol. 17, no. 7, pp. 1354–1358, Jul. 2018.

[37] A. A. Baba, R. M. Hashmi, K. P. Esselle, and A. R. Weily, "Compact high-gain antenna with simple all-dielectric partially reflecting surface," *IEEE Trans. Antennas Propag.*, vol. 66, no. 8, pp. 4343–4348, Aug. 2018.

[38] A. A. Baba, R. M. Hashmi, and K. P. Esselle, "Achieving a large gain-bandwidth product from a compact antenna," *IEEE Trans. Antennas Propag.*, vol. 65, no. 7, pp. 3437–3446, Jul. 2017.

[39] R. M. Hashmi and K. P. Esselle, "A class of extremely wideband resonant cavity antennas with large directivity-bandwidth products," *IEEE Trans. Antennas Propag.*, vol. 64, no. 2, pp. 830–835, Feb. 2016.

[40] A. Lalbakhsh, M. U. Afzal, K. P. Esselle, and S. L. Smith, "Wideband near-field correction of a Fabry–Pérot resonator antenna," *IEEE Trans. Antennas Propag.*, vol. 67, no. 3, pp. 1975–1980, Mar. 2019.

[41] W. Pan, C. Huang, P. Chen, X. Ma, C. Hu, and X. Luo, "A low-RCS and high-gain partially reflecting surface antenna," *IEEE Trans. Antennas Propag.*, vol. 62, no. 2, pp. 945–949, Feb. 2014.

[42] Y. Jia, Y. Liu, W. Zhang, J. Wang, S. Gong, and G. Liao, "High-gain Fabry–Pérot antennas with wideband low monostatic RCS using phase gradient metasurface," *IEEE Access*, vol. 7, pp. 4816–4824, 2019.

[43] H. Jiang, Z. Xue, M. Leng, W. Li, and W. Ren, "Wideband partially reflecting surface antenna with broadband RCS reduction," *IET Microw., Antennas Propag.*, vol. 12, no. 6, pp. 941–946, May 2018.

[44] J. Mu, H. Wang, H. Wang, and Y. Huang, "Low-RCS and gain enhancement design of a novel partially reflecting and absorbing surface antenna," *IEEE Antennas Wireless Propag. Lett.*, vol. 16, pp. 1903–1906, Mar. 2017.

[45] Y. Zheng, J. Gao, Y. Zhou, X. Cao, H. Yang, S. Li, and T. Li, "Wideband gain enhancement and RCS reduction of Fabry–Pérot resonator antenna with chessboard arranged metamaterial superstrate," *IEEE Trans. Antennas Propag.*, vol. 66, no. 2, pp. 590–599, Feb. 2018.

[46] Y.-J. Zheng, J. Gao, X.-Y. Cao, S.-J. Li, and W.-Q. Li, "Wideband RCS reduction and gain enhancement microstrip antenna using chessboard configuration superstrate," *Microw. Opt. Technol. Lett.*, vol. 57, no. 7, pp. 1738–1741, Jul. 2015.

[47] K. Li, Y. Liu, Y. Jia, and Y. J. Guo, "A circularly polarized high-gain antenna with low RCS over a wideband using chessboard polarization conversion metasurfaces," *IEEE Trans. Antennas Propag.*, vol. 65, no. 8, pp. 4288–4292, Aug. 2017.

[48] M. Long, W. Jiang, and S. Gong, "Wideband RCS reduction using polarization conversion metasurface and partially reflecting surface," *IEEE Antennas Wireless Propag. Lett.*, vol. 16, pp. 2534–2537, Jul. 2017.

[49] G. Perez-Palomino, J. E. Page, M. Arrebola, and J. A. Encinar, "A design technique based on equivalent circuit and coupler theory for broadband linear to circular polarization converters in reflection or transmission mode," *IEEE Trans. Antennas Propag.*, vol. 66, no. 5, pp. 2428–2438, May 2018.

[50] C. V. Vinisha, P. S. Mohammed Yazeen, P. Mahima, V. Joy, and R. U. Nair, "Multi-layered graded porous radome design for dual-band airborne radar applications," *Electron. Lett.*, vol. 53, no. 3, pp. 189–191, Feb. 2017.

[51] V. K. Kothapudi and V. Kumar, "A 6-Port two-dimensional 3×3 series-fed planar array antenna for dual-polarized X-Band airborne synthetic aperture radar applications," *IEEE Access*, vol. 6, pp. 12001–12007, 2018.

[52] B. Lund, H. C. Graber, and R. Romeiser, "Wind retrieval from shipborne nautical X-Band radar data," *IEEE Trans. Geosci. Remote Sens.*, vol. 50, no. 10, pp. 3800–3811, Oct. 2012.

[53] Y. Liu, W. Huang, E. W. Gill, D. K. Peters, and R. Vicen-Bueno, "Comparison of algorithms for wind parameters extraction from shipborne X-Band marine radar images," *IEEE J. Sel. Topics Appl. Earth Observ. Remote Sens.*, vol. 8, no. 2, pp. 896–906, Feb. 2015.

[54] J. P. Comeau, M. A. Morton, W.-M.-L. Kuo, T. Thrivikraman, J. M. Andrews, C. M. Grens, J. D. Cressler, J. Papapolymerou, and M. Mitchell, "A silicon-germanium receiver for X-Band transmit/receive radar modules," *IEEE J. Solid-State Circuits*, vol. 43, no. 9, pp. 1889–1896, Sep. 2008.

[55] N. Hernández, J. L. G. Rodríguez, J. A. Martin, F. S. R. Mata, González, and R. Álvarez, "An approach to automatic target recognition in radar images using SVM," in *Iberoamerican Congress on Pattern Recognition*, Berlin, Germany: Springer, Nov. 2006, pp. 964–973.

[56] Sarika, M. R. Tripathy, and D. Ronnow, "Dual band frequency selective surface for X-band applications," in *Proc. Electromagn. Res. Symp. (PIERS)*, Aug. 2016, pp. 5039–5042.

ZHIMING LIU was born in Jiangxi, China, in 1989. He received the B.S degree from the East China Institute of Technology, Fuzhou, China, in 2012, the M.S. degree from Nanchang University, Nanchang, China, in 2015, and the Ph.D. degree from the College of Electronic and Information Engineering, Nanjing University of Aeronautics and Astronautics, Nanjing, China, in 2019. He is currently a Postdoctoral Research Fellow with the Department of Electrical and Computer Engineering, University of Victoria, Victoria, BC, Canada. His current research interests include antennas and metasurface.

SHAOBIN LIU (Member, IEEE) received the Ph.D. degree in electronics science and technology from the National University of Defense Technology, in 2004. In 2003, he was promoted as a Professor. He is currently a Professor of electromagnetic and microwave technology with the Nanjing University of Aeronautics and Astronautics. His research focuses on plasma stealthy antennas, microwave, radio frequency, and electromagnetic compatibility.

JENS BORNEMANN (Life Fellow, IEEE) received the Dipl.-Ing. and Dr.-Ing. degrees in electrical engineering from the University of Bremen, Germany, in 1980 and 1984, respectively.

From 1984 to 1985, he worked as an Engineering Consultant. In 1985, he joined the University of Bremen, as an Assistant Professor. Since April 1988, he has been with the Department of Electrical and Computer Engineering, University of Victoria, Victoria, BC, Canada, where he became a Professor, in 1992. From 1992 to 1995, he was a Fellow of the British Columbia Advanced Systems Institute. In 1996, he was a Visiting Scientist with Spar Aerospace Limited (now MDA Space), Ste-Anne-de-Bellevue, Québec, Canada, and a Visiting Professor with the Microwave Department, University of Ulm, Germany. From 1997 to 2002, he was the Co-Director of the Center for Advanced Materials and Related Technology (CAMTEC), University of Victoria. In 2003, he was a Visiting Professor with the Laboratory for Electromagnetic Fields and Microwave Electronics, ETH Zurich, Switzerland. He is currently a Registered Professional Engineer with the Province of British Columbia, Canada. He has coauthored Waveguide Components for Antenna Feed Systems-Theory and Design (Artech House, 1993) and has authored/coauthored more than 350 technical articles. His research activities include RF/wireless/ microwave/millimeter-wave components and systems design, and field-theory-based modeling of integrated circuits, feed networks, and antennas. He is a Fellow of the Canadian Academy of Engineering (CAE) and the Engineering Institute of Canada (EIC), He serves on the editorial advisory board of the *International Journal of Numerical Modeling*. From 1999 to 2009, he has served on the Technical Program Committee of the IEEE MTT-S International Microwave Symposium. From 1999 to 2002, he has served as an Associate Editor of the IEEE TRANSACTIONS ON MICROWAVE THEORY AND TECHNIQUES in the area of microwave modeling and CAD. From 2006 to 2008, he was an Associate Editor of the *International Journal of Electronics and Communications*.

XING ZHAO was born in Tianjin, China. He received the B.Eng. degree in information engineering from Shanghai Jiao Tong University, Shanghai, China, in 2008, and the M.S. and Ph.D. degrees in electronics and computer engineering from Hanyang University, Seoul, South Korea, in 2010 and 2014, respectively.

From 2015 to 2017, he was a Postdoctoral Research Fellow with the Department of Electrical and Computer Engineering, National University of Singapore, Singapore. He is currently an Associate Research Fellow with the College of Electronic and Information Engineering, Nanjing University of Aeronautics and Astronautics, China. His current research interests include small antennas for 5G mobile MIMO platforms and integrated array antennas for radar systems.
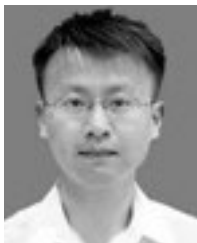
XIANGKUN KONG (Member, IEEE) received the Ph.D. degree in communication and information systems from the Nanjing University of Aeronautics and Astronautics (NUAA), in 2015. He has been an Associate Professor with NUAA, since his promotion in July 2015. He used to work at the University of St Andrews, U.K., as an Academic Visitor supported by the China Scholarship Council. His main research interests include the electromagnetic properties of metamaterials, metamaterials and metasurface application, plasma photonic crystal, and computational electromagnetics. He has published more than 100 articles in different academic journals, including *Applied Physics Letters*, *Optics Express*, and the IEEE JOURNAL OF SELECTED TOPICS IN QUANTUM ELECTRONICS. He has been cited 1600 times.

ZHENGYU HUANG was born in Hunan, China, in 1986. He received the B.S. degree in electronic and information engineering from Nanchang University, Nanchang, China, in 2008, and the Ph.D. degree in electromagnetic environmental effects and electro-optical engineering from the PLA University of Science and Technology, Nanjing, China, in 2016.

He is currently an Associated Professor with the Key Laboratory of Radar Imaging and Microwave Photonics, Nanjing University of Aeronautics and Astronautics, Nanjing. He has coauthored one monograph on the Associated Hermite finite-difference time-domain method and 30 peer-reviewed journal articles included in the *Web of Science Core Collection*. His research interests include computational electromagnetics, electromagnetic compatibility, and multiphysics modeling and analysis. He was a recipient of the Outstanding Doctoral Dissertation Award of the PLA University of Science and Technology, in 2017, and the Excellent Doctoral Dissertation Award by Lu Zhitao Academician, in 2018.
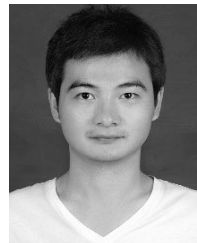
BORUI BIAN was born in Jiangsu, China, in 1985. He received the B.S. degree from Nanjing Tech University, in 2007, and the M.S. degree from the Nanjing University of Aeronautics and Astronautics, in 2012, where he is currently pursuing the Ph.D. degree with the College of Electronic and Information Engineering. His research interests include microwave devices design, metamaterial absorber, and low-RCS antenna design.
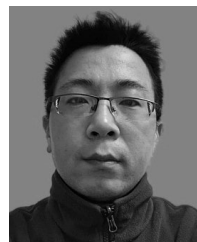
DONGDONG WANG was born in Henan, China, in 1984. He received the B.S. and M.S. degrees in electrical and electronic engineering from the Huazhong University of Science and Technology, Hubei, China, in 2006 and 2008, respectively, and the Ph.D. degree in physical electronics from Fudan University, Shanghai, in 2011. He was granted with the IEEE Tom R. Burks Exceptional Graduate Student Award for his contributions in the development of all-solid-state pulsed power systems, Atlanta, in 2010. He is currently working with the Science and Technology on Electromagnetic Compatibility Laboratory, China Ship Development and Design Center. His main research interests include electromagnetic environment effect simulation and experiments, and electromagnetic pulses, and lightning protection of different types of RF front ends.

• • •